Multi-channel medical device for time domain functional near infrared spectroscopy based on wavelength space multiplexing

Rebecca Re,[1,*] Davide Contini,[1] Massimo Turola,[2] Lorenzo Spinelli,[3] Lucia Zucchelli,[1] Matteo Caffini,[4] Rinaldo Cubeddu,[1] and Alessandro Torricelli[1]

[1]*Politecnico di Milano, Dipartimento di Fisica, Piazza Leonardo da Vinci 32, 20133 Milan, Italy*
[2]*Division of Optometry and Visual Sciences, City University London, Northampton Square, EC1V 0HB London, UK*
[3]*IFN-CNR, Piazza Leonardo da Vinci 32, 20133 Milano, Italy*
[4]*Politecnico di Milano, Dipartimento di Elettronica, Informazione e Bioingegneria, Via Golgi 39, 20133 Milan, Italy*
[*]*rebecca.re@mail.polimi.it*

Abstract: We have designed a compact dual wavelength (687 nm, 826 nm) multi-channel (16 sources, 8 detectors) medical device for muscle and brain imaging based on time domain functional near infrared spectroscopy. The system employs the wavelength space multiplexing approach to reduce wavelength cross-talk and increase signal-to-noise ratio. System performances have been tested on homogeneous and heterogeneous tissue phantoms following specifically designed protocols for photon migration instruments. Preliminary *in vivo* measurements have been performed to validate the instrument capability to monitor hemodynamic parameters changes in the arm muscle during arterial occlusion and in the adult head during a motor task experiment.

©2013 Optical Society of America

References and links

1. M. Ferrari and V. Quaresima, "A brief review on the history of human functional near-infrared spectroscopy (fNIRS) development and fields of application," Neuroimage **63**(2), 921–935 (2012).
2. D. Contini, L. Zucchelli, L. Spinelli, M. Caffini, R. Re, A. Pifferi, R. Cubeddu, and A. Torricelli, "Review: Brain and muscle near infrared spectroscopy/imaging techniques," J. Near Infrared Spectrosc. **20**(1), 15–27 (2012).
3. M. Wolf, M. Ferrari, and V. Quaresima, "Progress of near-infrared spectroscopy and topography for brain and muscle clinical applications," J. Biomed. Opt. **12**(6), 062104 (2007).
4. A. Torricelli, D. Contini, A. Pifferi, M. Caffini, R. Re, L. Zucchelli and L. Spinelli, "Time domain functional NIRS imaging for human brain mapping," Neuroimage (Available online 5 June 2013).
5. J. Steinbrink, H. Wabnitz, H. Obrig, A. Villringer, and H. Rinneberg, "Determining changes in NIR absorption using a layered model of the human head," Phys. Med. Biol. **46**(3), 879–896 (2001).
6. J. Selb, D. K. Joseph, and D. A. Boas, "Time-gated optical system for depth-resolved functional brain imaging," J. Biomed. Opt. **11**(4), 044008 (2006).
7. D. Contini, A. Torricelli, A. Pifferi, L. Spinelli, and R. Cubeddu, "Novel method for depth-resolved brain functional imaging by time-domain NIRS," Proc. SPIE **6629**, 662908, 662908-7 (2007).
8. A. Liebert, H. Wabnitz, J. Steinbrink, H. Obrig, M. Möller, R. Macdonald, A. Villringer, and H. Rinneberg, "Time-resolved multidistance near-infrared spectroscopy of the adult head: intracerebral and extracerebral absorption changes from moments of distribution of times of flight of photons," Appl. Opt. **43**(15), 3037–3047 (2004).
9. E. Kirilina, A. Jelzow, A. Heine, M. Niessing, H. Wabnitz, R. Brühl, B. Ittermann, A. M. Jacobs, and I. Tachtsidis, "The physiological origin of task-evoked systemic artefacts in functional near infrared spectroscopy," Neuroimage **61**(1), 70–81 (2012).
10. H. Wabnitz, M. Möller, A. Liebert, A. Walter, R. Erdmann, O. Raitza, C. Drenckhahn, J. Dreier, H. Obrig, J. Steinbrink, and R. Macdonald, "A time-domain NIR brain imager applied in functional stimulation experiments," Proc. SPIE **5859**, 58590H, 58590H-9 (2005).
11. H. Wabnitz, M. Moeller, A. Liebert, H. Obrig, J. Steinbrink, and R. Macdonald, "Time-resolved near-infrared spectroscopy and imaging of the adult human brain," Adv. Exp. Med. Biol. **662**, 143–148 (2010).

12. A. Liebert, H. Wabnitz, J. Steinbrink, M. Möller, R. Macdonald, H. Rinneberg, A. Villringer, and H. Obrig, "Bed-side assessment of cerebral perfusion in stroke patients based on optical monitoring of a dye bolus by time-resolved diffuse reflectance," Neuroimage **24**(2), 426–435 (2005).
13. O. Steinkellner, C. Gruber, H. Wabnitz, A. Jelzow, J. Steinbrink, J. B. Fiebach, R. Macdonald, and H. Obrig, "Optical bedside monitoring of cerebral perfusion: technological and methodological advances applied in a study on acute ischemic stroke," J. Biomed. Opt. **15**(6), 061708 (2010).
14. A. Liebert, H. Wabnitz, H. Obrig, R. Erdmann, M. Möller, R. Macdonald, H. Rinneberg, A. Villringer, and J. Steinbrink, "Non-invasive detection of fluorescence from exogenous chromophores in the adult human brain," Neuroimage **31**(2), 600–608 (2006).
15. A. Jelzow, H. Wabnitz, H. Obrig, R. Macdonald, and J. Steinbrink, "Separation of indocyanine green boluses in the human brain and scalp based on time-resolved in-vivo fluorescence measurements," J. Biomed. Opt. **17**(5), 057003 (2012).
16. M. Kacprzak, A. Liebert, P. Sawosz, N. Zolek, and R. Maniewski, "Time-resolved optical imager for assessment of cerebral oxygenation," J. Biomed. Opt. **12**(3), 034019 (2007).
17. M. Kacprzak, A. Liebert, W. Staszkiewicz, A. Gabrusiewicz, P. Sawosz, G. Madycki, and R. Maniewski, "Application of a time-resolved optical brain imager for monitoring cerebral oxygenation during carotid surgery," J. Biomed. Opt. **17**(1), 016002 (2012).
18. A. Liebert, P. Sawosz, D. Milej, M. Kacprzak, W. Weigl, M. Botwicz, J. Mączewska, K. Fronczewska, E. Mayzner-Zawadzka, L. Królicki, and R. Maniewski, "Assessment of inflow and washout of indocyanine green in the adult human brain by monitoring of diffuse reflectance at large source-detector separation," J. Biomed. Opt. **16**(4), 046011 (2011).
19. J. C. Hebden, A. P. Gibson, T. Austin, R. M. Yusof, N. Everdell, D. T. Delpy, S. R. Arridge, J. H. Meek, and J. S. Wyatt, "Imaging changes in blood volume and oxygenation in the newborn infant brain using three-dimensional optical tomography," Phys. Med. Biol. **49**(7), 1117–1130 (2004).
20. T. Austin, A. P. Gibson, G. Branco, R. Md, Y. S. R. Arridge, J. H. Meek, J. S. Wyatt, D. T. Delpy, and J. C. Hebden, "Three-dimensional optical imaging of blood volume and oxygenation in the preterm brain," Neuroimage **31**(4), 1426–1433 (2006).
21. A. P. Gibson, T. Austin, N. L. Everdell, M. Schweiger, S. R. Arridge, J. H. Meek, J. S. Wyatt, D. T. Delpy, and J. C. Hebden, "Three-dimensional whole-head optical tomography of passive motor evoked responses in the neonate," Neuroimage **30**(2), 521–528 (2006).
22. J. C. Hebden, S. Magazov, N. Everdell, and M. Varela, "A time-domain system for optical tomography of the newborn infant brain," presented at nEUROPt Workshop, Non-invasive imaging of brain function and disease by pulsed near infrared light, Milan, 12–13 March 2012.
23. J. C. Hebden, M. Varela, S. Magazov, N. Everdell, A. Gibson, J. Meek, and T. Austin, "Diffuse optical imaging of the newborn infant brain," in Proceeding. of 9th IEEE International Symposium onBiomedical Imaging: from Nano to Macro, Barcelona, 2–5 May 2012.
24. J. Selb, J. J. Stott, M. A. Franceschini, A. G. Sorensen, and D. A. Boas, "Improved sensitivity to cerebral hemodynamics during brain activation with a time-gated optical system: analytical model and experimental validation," J. Biomed. Opt. **10**(1), 011013 (2005).
25. J. Selb and D. A. Boas, "A Second Generation Time-Domain Imaging System from MGH," presented at nEUROPt Workshop, Non-invasive imaging of brain function and disease by pulsed near infrared light, Milan, 12–13 March 2012.
26. J. Selb, B. B. Zimmermann, M. Martino, T. M. Ogden, and D. A. Boas, "Functional brain imaging with a supercontinuum time-domain NIRS system," Proc. SPIE **8578**, 857807 (2013).
27. M. Diop, K. M. Tichauer, J. T. Elliott, M. Migueis, T.-Y. Lee, and K. St. Lawrence, "Time-resolved near-infrared technique for bedside monitoring of absolute cerebral blood flow," Proc. SPIE **7555**, 75550Z (2007).
28. R. Re, D. Contini, M. Caffini, R. Cubeddu, L. Spinelli, and A. Torricelli, "A compact time-resolved system for near infrared spectroscopy based on wavelength space multiplexing," Rev. Sci. Instrum. **81**(11), 113101 (2010).
29. D. Contini, A. Torricelli, A. Pifferi, L. Spinelli, F. Paglia, and R. Cubeddu, "Multi-channel time-resolved system for functional near infrared spectroscopy," Opt. Express **14**(12), 5418–5432 (2006).
30. A. Pifferi, A. Torricelli, A. Bassi, P. Taroni, R. Cubeddu, H. Wabnitz, D. Grosenick, M. Möller, R. Macdonald, J. Swartling, T. Svensson, S. Andersson-Engels, R. L. P. van Veen, H. J. Sterenborg, J. M. Tualle, H. L. Nghiem, S. Avrillier, M. Whelan, and H. Stamm, "Performance assessment of photon migration instruments: the MEDPHOT protocol," Appl. Opt. **44**(11), 2104–2114 (2005).
31. H. Wabnitz, A. Jelzow, M. Mazurenka, O. Steinkellner, R. Macdonald, A. Pifferi, A. Torricelli, D. Contini, L. Zucchelli, L. Spinelli, R. Cubeddu, D. Milej, N. Zolek, M. Kacprzak, A. Liebert, S. Magazov, J. Hebden, F. Martelli, P. Di Ninni and G. Zaccanti, "Performance assessment of time-domain optical brain imagers: The neuropt protocol," *In Biomedical Optics*, Technical Digest (Optical Society of America, 2012), paper BSu2A.4.
32. International Elettrotechnical Commision, IEC 60825–1:2007, Edition 2. Safety of Laser Products - Part 1: Equipment Classification and Requirements (2007).
33. H. Wabnitz, A. Pifferi, A. Torricelli, D. R. Taubert, M. Mazurenka, O. Steinkellner, A. Jelzow, A. Farina, I. Bargigia, D. Contini, M. Caffini, L. Zucchelli, L. Spinelli, P. Sawosz, A. Liebert, R. Macdonald, and R. Cubeddu, "Assessment of basic instrumental performance of time-domain optical brain imagers," Proc. SPIE **7896**, 789602, 789602-8 (2011).
34. D. Contini, F. Martelli, and G. Zaccanti, "Photon migration through a turbid slab described by a model based on diffusion approximation. I. Theory," Appl. Opt. **36**(19), 4587–4599 (1997).

35. L. Spinelli, F. Martelli, A. Farina, A. Pifferi, A. Torricelli, R. Cubeddu, and G. Zaccanti, "Accuracy of the nonlinear fitting procedure for time-resolved measurements on diffusive phantoms at NIR wavelengths," Proc. SPIE **7174**, 717424, 717424-10 (2009).
36. A. Torricelli, L. Spinelli, J. Kaethner, J. Selbeck, A. Franceschini, P. Rozzi, and M. Zude, "Non-destructive optical assessment of photon path lengths in fruit during ripening: implications on design of continuous-wave sensors," International Conference Of Agricultural Engineering, CIGR-AgEng2012,Valencia 8–12 July 2012, Papers Book, ISBN-10 84–615–9928–4.
37. W. Louisell, Quantum Statistical Properties of Radiation (Wiley, New York, 1973).
38. F. Martelli, A. Pifferi, D. Contini, L. Spinelli, A. Torricelli, H. Wabnitz, R. Macdonald, A. Sassaroli, and G. Zaccanti, "Phantoms for diffuse optical imaging based on totally absorbing objects, part 1: basic concepts," J. Biomed. Opt. **18**(6), 066014 (2013).
39. L. Spinelli, F. Martelli, A. Farina, A. Pifferi, A. Torricelli, R. Cubeddu, and G. Zaccanti, "Calibration of scattering and absorption properties of a liquid diffusive medium at NIR wavelengths. Time-resolved method," Opt. Express **15**(11), 6589–6604 (2007).
40. S. Del Bianco, F. Martelli, F. Cignini, G. Zaccanti, A. Pifferi, A. Torricelli, A. Bassi, P. Taroni, and R. Cubeddu, "Liquid phantom for investigating light propagation through layered diffusive media," Opt. Express **12**(10), 2102–2111 (2004).
41. J. C. Ye, S. Tak, K. E. Jang, J. Jung, and J. Jang, "NIRS-SPM: Statistical parametric mapping for near-infrared spectroscopy," Neuroimage **44**(2), 428–447 (2009).
42. http://bisp.kaist.ac.kr/NIRS-SPM.html.

1. Introduction

Functional near infrared spectroscopy (fNIRS) is an optical technique that noninvasively measures the concentration of oxygenated hemoglobin (O_2Hb) and deoxygenated hemoglobin (HHb) in the muscle and in the brain [1,2]. While the continuous wave (CW) approach to fNIRS is widely adopted in both research and clinical applications, in the biomedical community there is an increasing interest for time domain (TD) fNIRS [3,4]. TD fNIRS exploits the temporal information encoded in the photon distribution of time-of-flight (DTOF): in particular, in the reflectance geometry where source and collection fibers are placed on the same surface, photons which stay longer in the tissue have a higher probability of exploring deeper regions, while photons that arrive earlier at the detector had very likely traveled only through the more superficial tissue's layers. By applying proper physical models it is then possible to discriminate between the superficial and the deeper contributions to the fNIRS signal [5–8]. This is of the utmost importance for example in muscle applications where the presence of a superficial adipose tissue may induce large errors in the estimate of the absolute values of O_2Hb and HHb of the underlying muscle. More importantly, TD fNIRS can be of help in brain applications where the superficial signals originated by systemic or task related changes can eventually mask the underlying brain cortex activity [9].

The basic features of TD fNIRS and the characteristics of the existing TD fNIRS systems have been recently reviewed by the Authors [4]. It is worth mentioning that European research groups located in academic or public research centers have designed and built most of the existing TD fNIRS systems effectively employed in the clinics. In particular the most active in the field are the research groups at Physikalisch-Technische Bundesanstalt, Berlin, Germany [9–15], at the Institute of Biocybernetics and Biomedical Engineering, Warsaw, Poland [16–18], and at the the Department of Medical Physics and Bioengineering, University College London [19–23]. In the US we can mention the group at the Massachusetts General Hospital, Athinoula A. Martinos Center, Charlestown, Massachusetts [6, 24–26]. In Canada we can mention the group at the University of Western Ontario, Department of Medical Biophysics London, Ontario [27].

In this paper we aim at presenting in details the design and the characterization of a novel dual-wavelength multi-channel TD fNIRS compact system. The system adopts a couple of picosecond light sources, a multi-channel fiber optic switch to deliver light into the tissue, and a detection unit consisting of eight independent chains for time-correlated single photon counting (TCSPC). While this is a standard scheme for TD fNIRS systems, we have adopted innovative solutions to improve the performances of the system. In particular the system is based on the wavelength space multiplexing scheme previously introduced by the Authors [28] to increase the signal-to-noise ratio (SNR) and reduce the wavelength cross-talk with

respect to the existing instrument based on the wavelength time multiplexing scheme [29]. This is the first example of TD fNIRS multi-channel instrument based on wavelength space multiplexing that can be used for imaging purposes. Moreover, in the acquisition TCSPC chains we have adopted newly developed hybrid photomultipliers with reduced after-pulsing background and we have avoided the use of electronic routers to multiplex the signals from different channels, so as to increase the overall dynamic range. Further, we report on a comprehensive characterization of the system that goes beyond the classical Medphot protocol based on homogeneous phantoms [30] but adopts the more recently developed nEUROPt protocol [31] specifically designed to test the performances of a TD fNIRS system in a heterogeneous medium. Finally, we present preliminary *in vivo* measurements on human arm muscle and head to highlight the features of the developed TD fNIRS system. For the muscle measurements we provide oxy- (O_2Hb) and deoxy-hemoglobin (HHb) time courses. For the brain monitoring we present the contrast for the intensity, O_2Hb and HHb time courses and statistical parametric maps (SPM) of the cortical activations.

2. System setup

The developed system is based on the wavelength space multiplexing approach: the different wavelengths are alternatively injected into the sample in order to acquire in each detection line only one DTOF, at one wavelength, at a time. In this way it is possible not only to completely avoid the wavelength cross-talk, but also to increase the instrument SNR [28].

The system was designed with a modularity structure: six different drawers were housed in a 19" rack case (116 x 60 x 60 cm) in order to divide out the different instrument sections and to guarantee simplicity in case of replacement or upgrade of the modules. This solution is particularly suitable for a clinical environment, where portability, compactness and robustness are required. The different modules are divided in: power supply, injection, detection, acquisition, and control, as described below. The system is also equipped with temperature controlled fans to allow heat exchanges and prevent instrument overheating. In Fig. 1(a) and 1(b) a schematic of the instrument and a photo of the final arrangement are shown.

Power supply module: a de-coupling transformer (REOMED 1000BV, Reo Italia s.r.l., Italy) provides 9 higher voltage outlets (115 V or 220 V input, selectable with a switch, 220 V output) isolating the instrument from the external main supply and protecting the room electrical system from possible instrument malfunctioning. A switching power pack provides 4 lower voltage outlets (12 V). In this way the needed power can be delivered to the different sections. An interlock unit is also installed for the fast instrument power off as required by safety regulations. This module is also equipped with a Global System for Mobile Communications (GSM) switch unit to remotely turn on and off the instrument, useful for managing the instrument warm-up.

Injection module: a couple of compact picosecond pulsed diode laser operating at 687 nm and 826 nm, with pulse duration of about 50 ps FWHM, pulse repetition rate of 80 MHz, average power <1 mW, were employed as light sources (LDH-P, SEPIA II, PicoQuant GmbH, Germany). The laser power is controlled with a custom-made attenuation and equalization stage based on micrometric shutters and stepper motors electronically controlled by the microcontroller unit. The attenuation stage is necessary to equalize and control the power delivered into the different channels. An optical switch (2x18 mol, Leoni Fiber Optics GmbH, Germany) allows the implementation of the wavelength space multiplexing approach and the
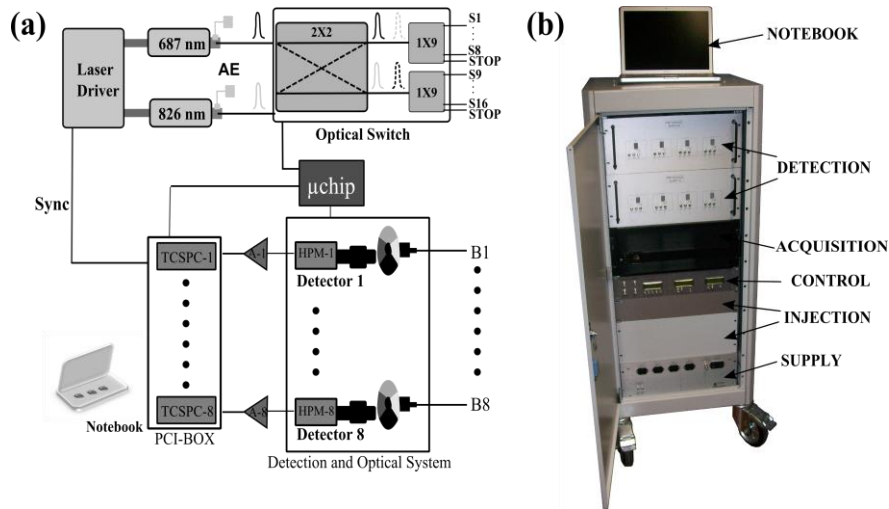
Fig. 1. (a) Complete scheme of the system. AE: Attenuation-Equalization stage; S: injection fiber; B: collection bundle; HPM: hybrid photomultiplier tube; A: amplifier; TCSPC: time correlated single photon counting board; μchip: microcontroller unit; Sync: synchronization signal. (b) Photo of the medical device with modules description.

extension of the injection channels from 2 up to 16. The 2x18 switch consists of a cascade of a 2x2 and two 1x9 switches in parallel as indicated in Fig. 1(a). The 2x2 switch redirects the light pulses at λ_1 in the first 1x9 switch, and the light pulses at λ_2 in the other 1x9 switch. First the 1x9 switches operate in parallel to inject light in all corresponding source fibers (i.e. in parallel in the left and right hemisphere). Then the 2x2 switch swaps the wavelengths and the 1x9 switches repeat the procedure. For a fixed acquisition time Δt_A (i.e. the time to acquire the data from all channels at both wavelengths), the switching time of the 2x2 switch is $\Delta t_{S2x2} = \Delta t_A/2$. The switching time of the 1x9 switches is $\Delta t_{S1x9} = \Delta t_{S2x2}/N_S$, where N_S is the number of sources to be addressed in each hemisphere. Typically $\Delta t_A = 1$s so as to properly monitor the hemodynamic response, and $N_S = 5$ (as in the *in vivo* results that will be presented in this paper), therefore typical values are $\Delta t_{S2x2} = 0.5$ s and $\Delta t_{S1x9} = 0.1$ s. Two channels are used as stop channel for safety purposes. After the optical switch, the laser light is injected into the tissue by means of graded index multimode glass optical fibers with 100/140 μm of core/cladding and a numerical aperture of 0.29 (Lightec s.r.l., Italy). At the end of the injection fibers a spacer was inserted in order to enlarge the laser spot size maintaining the optical power density <2 mW/mm^2 accordingly to the safety threshold [32].

Detection module: Eight identical and independent detection lines were implemented. In each line, light is collected after the sample by means of custom-made glass optical fiber bundles (Loptek Glasfasertechnick GmbH, Germany) with an inner diameter of 3 mm and a numerical aperture of 0.57. In each line a hybrid photomultiplier tube (H-PMT) is employed to eliminate the after-pulsing phenomenon and to increase the achievable detector dynamic range (HPM-100-50, Becker & Hickl GmbH, Germany). After a motorized attenuation stage (step-variable neutral density attenuators, Thorlabs, NDC-50S, Newton, NJ, USA) light is coupled to the H-PMT active area by means of a proper lens system. This is composed of two aspheric lenses with a focal length of 18.75 mm (NT-49113, Edmund Optics GmbH, Germany). A custom double band-pass optical filter (OPMI-0037, Semrock, Rochester, NY, USA), centered at 687 nm and 826 nm, was inserted to decrease the background due to the ambient light. The H-PMT is also protected by means of an electronically driven shutter (DSS25B1T0-CR122011SP1, Uniblitz, Rochester, NY, USA).

Acquisition module: after each detection block one independent board for TCSPC is inserted (SPC-130, Becker & Hickl GmbH, Germany). The eight boards are located inside a PCI box (P13M, Magma, San Diego, CA, USA), and controlled in remote by an external

notebook with Thunderbolt Interface. Inside the PCI box four control modules (DCC-100, Becker & Hickl GmbH, Berlin, Germany) are also hosted to control the eight H-PMT detectors. Before the TCSPC board the electrical signal is properly amplified (HAFC-26, Becker&Hickl GmbH, Germany).

Control module: The whole system is controlled by a series of home-made units based on microcontrollers (DSPIC, Microchip Technology Inc., Chandler, AZ, USA). Each unit can be controlled by software or manually. The microcontroller units drive all the actuators present in the system (attenuators, shutters and the switching unit). The synchronization and communication between the different microcontroller units is performed by means of the I2C protocol. Furthermore the control module guarantees during measurements the synchronization between the TCPSC acquisition boards and all the other parts of the instrument guaranteeing an independent and precise time-basis. The section is completed by an home-made software, written in C-language in the LabWindows/CVI environment (National Instruments, Austin, TX, USA). The module (and therefore the whole system) has the possibility to be synchronized with other medical systems (e.g. system for acquisition of peripheral physiological signals, EEG instruments, fMRI scanners).

3. System characterization

The system was characterized on calibrated homogeneous and heterogeneous phantoms by means of three different protocols specifically devised to test the performances of the instrument (hardware) and of the data analysis algorithms (software).

3.1 Basic Instrumental Performance (BIP)

The first step in the assessment of the performances of the TD fNIRS instrument (and in general of a photon migration instrument based on the TD approach) includes a number of basic tests performed in a direct way with minimum involvement of phantoms and data analysis and related to parameters of the source, the detection system, the timing electronics and the temporal instrument response function (IRF). The Basic Instrumental Performance (BIP) tests (responsivity, differential nonlinearity, shape of the IRF, stability) are described in details in Reference [33]. Here we just report the results for the developed system.

In Table 1 the source parameters for both wavelengths are summarized.

Table 1. Source characterization. λ = center wavelength, $\Delta\lambda$ = spectrum width, f_{rep} = laser repetition rate, $P_{av,out}$ = laser output power, P_{source} = laser power delivered to the sample at the source optode, A_{source} = illuminated area on the surface of the sample

λ [nm]	$\Delta\lambda$ [nm]	f_{rep} [MHz]	$P_{av,out}$ [mW]	P_{source} [mW]	A_{source}[mm^2]
687	3.4	80	0.936	0.577	7.5
826	5.2	80	0.266	0.163	7.5

The average responsivity over the 8 different detection channels is $(4.29 \pm 0.97)\cdot10^{-8}$ m^{2}sr and $(3.34 \pm 0.60)\cdot10^{-8}$ m^{2}sr, respectively for the wavelength at 687 nm and 826 nm.

The timing electronics present a good differential non linearity (DNL = 6.77%) showing a good uniformity of the time channels width in our TCSPC system.

For what concern the IRF, we found a FWHM of about 450 ps (400 ps) for the wavelength at 687 nm (826 nm). In Fig. 2(a), an example of the IRF at the two wavelengths is presented. It shows a dynamic range of more than four orders of magnitude (the time multiplexing instrument had a dynamic range of about three orders of magnitude [29], and the previous space-multiplexing two-channel instrument around four orders of magnitude [28]). The secondary peak is an internal reflection (with relative amplitude with respect to the IRF main peak of 1.7% at 687 nm and 1.5% at 826 nm) due to the optical bundles that can be easily eliminated during the data analysis processing. The average after-pulsing ratio (AR) over the detectors is (0.21 ± 0.17) % at 687 nm and (0.11 ± 0.15) % at 826 nm. This ratio relates the total counts in the background, after the subtraction of the dark background and rescaling to the full laser period, to the total counts in the signal [33]. As expected, these values are significantly lower than the ones found in our previous instrument (AR = 0.7%)

indicating that the H-PMTs allow to overcome the after-pulsing problem typical of the classical photomultiplier tube detectors.

Finally, in Fig. 2(b), the stability results for the photon counts and the photon mean time-of-flight of the IRF at 687 nm, referred to one detector, are shown. The counts vary by <5% over 420 min with a rather monotonic decrease. Approximately 100 min are needed to enter into the ± 1% range of the final average value calculated over of the last 30 min. The mean time-of-flight varies of about 250 ps over the 420 min, as shown in Fig. 2(b), and it becomes stable inside a ± 10 ps band after about 300 min, which has to be considered the system warm-up time. Similar results were in fact found for the other wavelength and the other detectors.
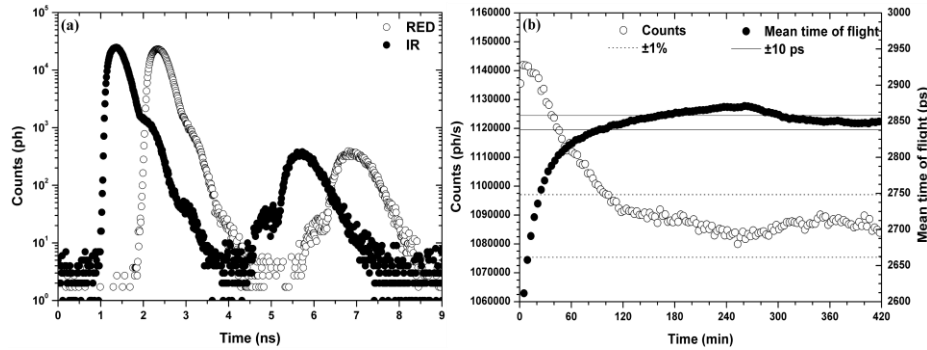
Fig. 2. (a): an example of IRF. RED = 687nm, IR = 826nm. (b): stability test for the counts and the photon mean time-of-flight of the IRF at 687 nm for one detector.

3.2 MEDPHOT protocol

The MEDPHOT protocol is a standard procedure of characterization which allows assessing the instrument's performances in terms of linearity, accuracy, noise, stability, and reproducibility [30]. It is also possible to compare different photon migration instruments in term of measurement performances, thanks to the employment of standard solid phantoms with different optical properties. Each phantom, based on epoxy resin with TiO_2 powder as the scatterer and black toner as the absorber, is recognizable by way of a label with a letter (A–D) and a number (1–8), which represent, respectively, the nominal reduced scattering (from 5 cm^{-1} to 20 cm^{-1}, in 5 cm^{-1} steps) and the nominal absorption (from 0 cm^{-1} to 0.49 cm^{-1}, in 0.07 cm^{-1} steps) coefficients at 660 nm. Taking into account the typical optical properties of human tissues (e.g. brain and muscle), we employed only a subgroup of the entire phantoms set: labels 2, 3, 4, and 5 for the absorption coefficient (nominal values 0.07, 014, 0.21, and 0.28 cm^{-1}) and labels A, B, and C for the reduced scattering coefficient (nominal values 5, 10, and 15 cm^{-1}). A simultaneous estimate of reduced scattering and absorption coefficients for each source-detector couple was achieved by best fitting of DTOFs with a standard model of the photon diffusion theory [34]. Fitting parameters have been chosen in order to optimize the accuracy of retrieved optical parameters [35]. We performed measurements in a reflectance geometry with one injection channel and eight detection lines at a source-detector distance of 30 mm.

Linearity and accuracy. We performed 10 repeated measurements on each phantom with an acquisition time of 1 s and a count rate of about 10^6 photon/s. The points in Fig. 3 and 4 refer to the average value over the repetitions and the detectors at 687 nm (similar results were found for 826 nm). The error bars are the corresponding standard deviations, which are mostly due to the inter-detector variability. In Fig. 3(a) the measured absorption versus the conventional true absorption coefficient, for phantom A, B, and C, is plotted. The conventional values have been measured by means of a TD NIRS instrument [36] which guarantees a good estimate of the optical parameters thanks to a narrow (about 200 ps), clean and stable IRF [35]. The lines are the linear fit. In Fig. 3(b) we plotted the measured reduced

scattering coefficients versus the true conventional ones. The solid lines are the linear fit of the measured points. For both coefficients the points are well aligned along the fit lines showing the goodness of our system linearity (average goodness of the fit: $R^2 = 0.998 \pm 0.001$ for the absorption and $R^2 = 0.998 \pm 0.002$ for the reduced scattering coefficient).
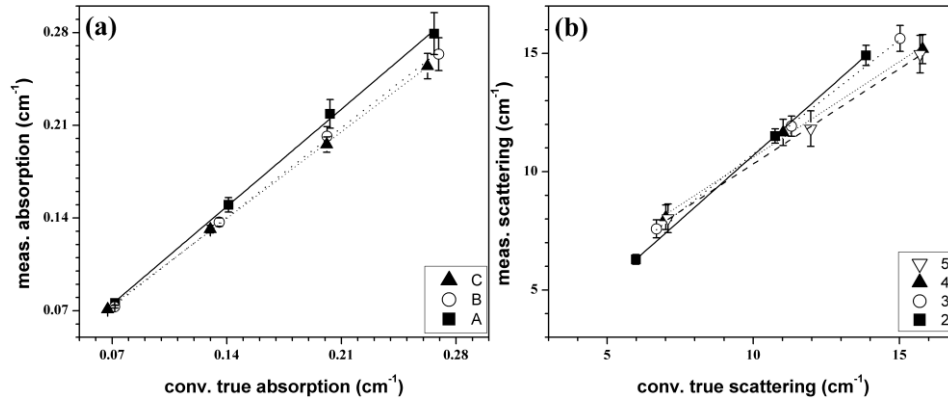

Fig. 3. Linearity for the absorption (a) and reduced scattering (b) coefficients at 687 nm. Results are average values over detectors and repeated measurements. The lines represent the linear fit.

In Fig. 4(a) and 4(b) the measured absorption and reduced scattering coefficients versus the nominal absorption and reduced scattering coefficients are respectively plotted. The solid lines link together the conventional values. We found an average relative error of about <4% for the absorption and <8% for the reduced scattering coefficients, showing a good accuracy in particular for the absorption coefficient.
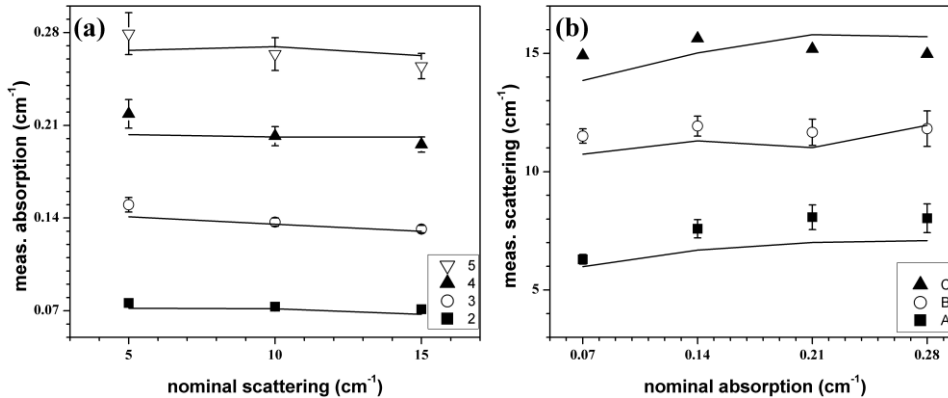

Fig. 4. Accuracy for the absorption (a) and reduced scattering (b) coefficients at 687 nm. Results are average values over detectors and repeated measurements. The lines link the conventional values.

Noise. In order to evaluate the minimum number of counts for a single reflectance curve, necessary to have an adequate SNR to perform data analysis, the coefficient of variation (CV) was calculated. We estimated the absorption and the reduced scattering coefficients with the same procedure we employed for the *in vivo* measurements (see section 4). For both wavelengths the CV for the absorption coefficient is lower than 1% already when the counts are only 10^4 photons. Conversely, for the reduced scattering coefficient we need at least $2 \cdot 10^5$ photons to reach the 1% level. In Fig. 5 the results for both coefficients and all detectors, at 687 nm, are shown. The lines in the graph represent the best fit of CV with the power function N^n, weighed on the variance. According to the photon noise statistics [37] we would

expect n = −0.5. We found n = −0.40 for the absorption and n = −0.52 for the reduced scattering coefficients. Similar results were found for the other wavelength.
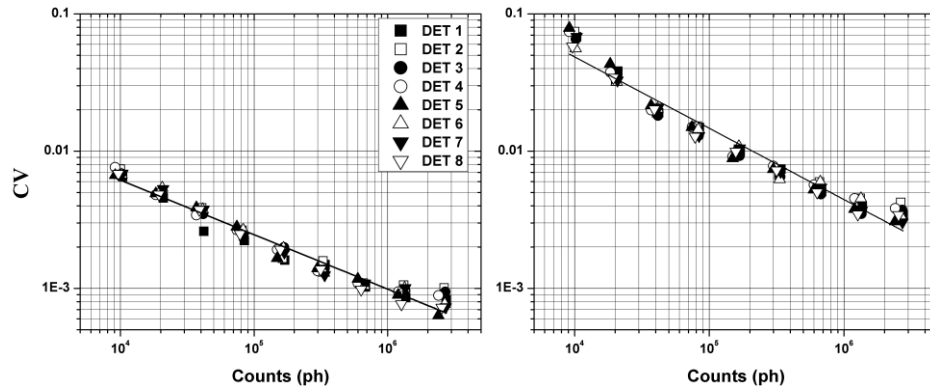

Fig. 5. CV for the absorption and the reduced scattering coefficient at 687 nm. Lines: best fit with a power function. DET: Detector.

Stability. The stability test, already performed for the IRF, was repeated on phantom B3. In this way it is possible to understand not only the instrument stability but also how this stability affects the optical properties estimation. The 7 hours long measurement confirmed the 300 min warm-up, found in the previous experiment, to have stability inside the ± 1% band (or 200 min for ± 3%). This period is mostly due to the laser head drifts.

Reproducibility. We tested the reproducibility of the coefficient's values estimated over three different days, performing the measurements in the same experimental conditions. We calculated the relative percentage error of the optical parameters with respect to the average over the days. We found, for both the coefficients at the two wavelengths, errors lower than 1% underlying an excellent reproducibility.

3.3 nEUROPt protocol

During the protocols described in the previous sections, we characterized our system in terms of technical features (BIP) and measurement performances (MEDPHOT) on homogeneous phantoms. The nEUROPt protocol instead aims at assessing the capability of a TD fNIRS system to measure optical quantities also on heterogeneous phantoms mimicking a real *in vivo* activation [4, 31, 38]. The whole data analyses were performed dividing the reflectance curve in time gates with fixed width (500 ps) and variable delay (from 500 ps to 4000 ps, in 500 ps steps). The protocol was implemented with liquid phantoms (μ_a = 0.1 cm^{-1}, μ_s' = 10.0 cm^{-1}, similar to the average human head optical properties) based on calibrated Intralipid and ink [39] with black inclusion (PVC cylinders of different sizes), mimicking a localized absorption perturbation to define penetration depth (i.e. the maximum depth at which the perturbation is recorded) and in a two-layered geometry to determine depth selectivity (i.e. the ability to discriminate a deep perturbation in the presence also of a superficial perturbation) . The protocol estimates the contrast, defined as $C(d,w;T;\lambda)$ = − $ln[N(d,w;T;\lambda)/N_0(d,w;\lambda)]$, where $N(d,w;T;\lambda)$ is the number of photons collected in a time window with delay d and width w, at macroscopic (experiment) time T for wavelength λ, and $N_0(d,w;\lambda)$ is the number of photons collected in the very same time window and for the same wavelength, averaged over the baseline period of the protocol.

Penetration depth. In this experiment a 100 mm^3 PVC black cylinder was placed in the mid plane between source and detector (source detector distance 30 mm) inside the liquid and moved in order to change its distance from the source-detector plane (depth from 6 mm to 30 mm, in 2 mm steps). In this way it is possible to mimic a typical change in the absorption coefficient at different depths inside the liquid. In Fig. 6(a) the contrast is plotted versus the inclusion depth for two different time gates and for the CW case (sum of photons detected at

any time). For the early time gate the contrast is high (>0.4) at small depth (<10 mm) but it rapidly decreases below 0.2 if the depth of the black object increases over 10 mm. The contrast for the CW case is similar to the early time gate but with shifted toward slightly larger depth (e.g. the contrast is <0.2 when the depth is >14 mm). Conversely for the late time gate the contrast increases from 0.4 to 0.7 when the depth of the inclusion increases from 6 mm to 14 mm, then it slowly diminishes (e.g. the contrast is <0.2 when the depth is >24 mm). To better understand this behavior, in Fig. 6(b), the dependence of the contrast from the photon time-of-flight is plotted for different depths. The deeper inclusions are detectable only at late time windows. For the inclusion at 30 mm of depth the contrast is close to zero for the time gates with a delay t < = 3000 ps. Only for the last time gate at t = 3200 ps the contrast is slightly positive, again confirming that the latter is the time gate the larger is the penetration depth.
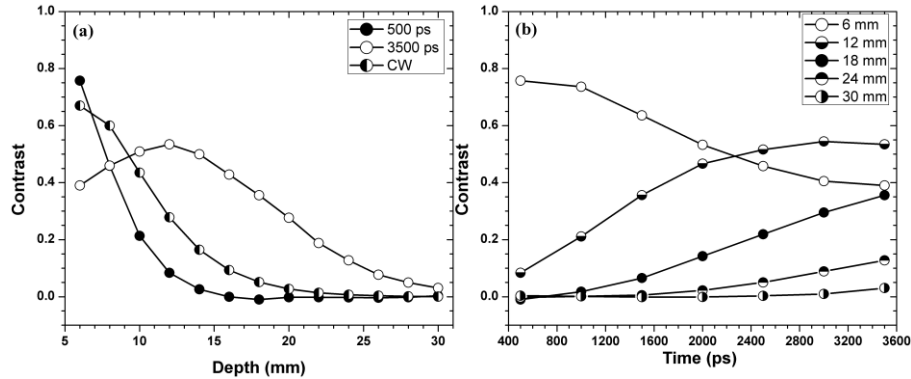

Fig. 6. (a) Contrast plotted against the inclusion depth at different time gates and in the CW case. (b) Contrast plotted against the photon time-of-flight for different inclusion depths.

Depth selectivity. A two layered liquid phantom (upper layer thickness: 10 mm, lower layer thickness: 40 mm) was prepared [40] and absorption changes were produced alternatively into the two layers, adding known amounts of black ink. In Fig. 7(a) the contrast is plotted against the absorption changes occurring only in the upper layer for different time gates. Conversely, Fig. 7(b) shows the case of changes only in the deeper layer. We can observe that an early time window (i.e. 500 ps delay, closed circles in Fig. 7(a) and 7(b)) is sensitive only to an absorption perturbation in the superficial layer, while a late time windows (i.e. >2000 ps delay, closed triangles in Fig. 7(a) and 7(b)) is sensitive to absorption perturbations in the deeper layer, but it is also affected by changes in the superficial layer (all injected photons must travel in the superficial layer before reaching the deeper layer and being eventually detected). It is possible to apply algorithms that exploits the information from early and late time gate to better estimate the changes in the optical properties in superficial and deeper structures of the tissue, such as the one proposed by Contini et al. [7]. As it is also shown in Fig. 7(a), in this way it is possible to avoid contaminations due to a perturbation occurring in the tissue's superficial layers (open circles in Fig. 7(a)), which during measurements on human subjects are typically caused by systemic hemodynamic activity.
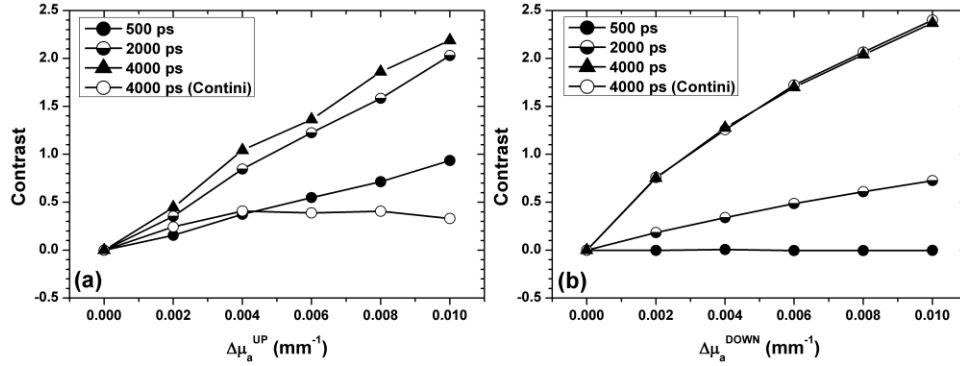
Fig. 7. Contrast as a function of the absorption coefficient variations occurring in the only upper (a) or deeper (b) layer of a two-layered medium for different time gates (500, 2000, 4000ps and 4000ps obtained with the correction proposed by Contini et al. [7].

4. *In vivo* applications

After the successful characterization on phantoms, we carried out preliminary *in vivo* measurements to monitor hemodynamic responses in the arm muscle during a cuff occlusion, and in the brain cortex during a handgrip movement.

4.1 Arterial cuff occlusion in the arm

A standard arterial cuff occlusion (180 mmHg) of the right arm muscle was performed on a subject. The protocol consists of: 60 s baseline (with no occlusion in both arms), 120 s occlusion (of the right arm only) and 180 s recovery (again with no occlusion in both arms), with a sampling time of 1 s. We placed one pad per each arm by means of a black rubber pad probe (1 source and 4 detectors, 30 mm interfiber distance). In Fig. 8 the time courses of the variations of the O_2Hb and HHb concentrations and of the oxygen saturation ($[SO_2]$ = $[O_2Hb]/([O_2Hb] + [HHb])$), on both arms, are plotted. We applied the correction method based on the use of early (0-1000 ps) and late time windows (2000-5000 ps) to enhance the contribution from deeper tissues [7]. The bars represent the standard deviation over the four measurement points. During the arterial occlusion the oxygenated blood cannot reach the occluded part (decrease in O_2Hb) and the de-oxygenated one cannot go out while the cells metabolism is not interrupted (increase in HHb), resulting in a SO_2 decreasing. After the occlusion period, we observe a peak in the hemodynamic parameters due to blood reperfusion after fast cuff release, then values returns around the baseline. Also for the left arm we can notice some small changes in the hemoglobin parameters. It is reasonable that a so big perturbation at the circulatory system caused by an arterial occlusion in one arm has some systemic effect. As a matter of fact, changes occurring in the left arm are smaller and show different pattern with respect to the occluded arm.
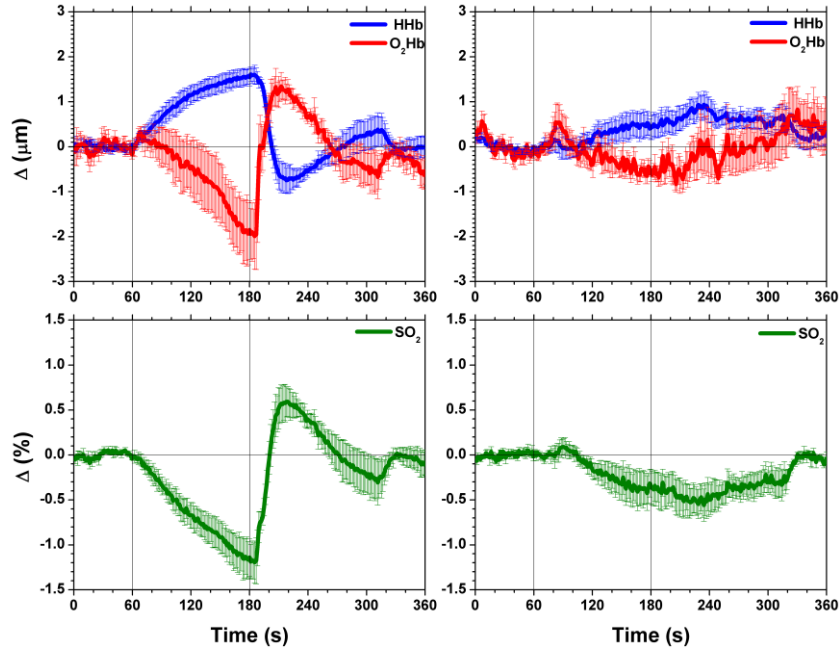
Fig. 8. Hemodynamic changes during an arterial cuff occlusion of the right arm. First column: right arm. Second column left arm. The bars represent the standard deviation over the four measurement points

4.2 Motor cortex response during hand grip

We monitored the hemodynamic cortical changes in O_2Hb and HHb on one adult volunteer during a motor task (right hand grip). A simple block designed protocol was considered consisting of six 40 s long trials: 10 s rest, 20 s hand gripping at self-pace, and 10 s recovery (at rest). A total of 12 measurement points per each hemisphere were recorded, by placing 5 injection (red circles) and 4 detection (green squares) fibers in each hemisphere around C3 and C4, respectively (see Fig. 9). Fibers were kept in place by a modified EEG cap (g.EEGcap, g-TEC, Austria). Source detector distance was on average 30 mm. The acquisition time was fixed to 1 s, by multiplexing the different injection fibers, in parallel for the two hemispheres, every 0.2 s. The count rate was fixed at 10^6 photon/s, on average in all channels.
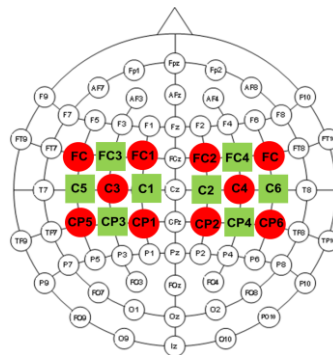

Fig. 9. Optodes positions on the head: 5 injections (red circles) and 4 detections (green squares) optical fibers, around left and right motor cortex points (C3 and C4).

Figure 10 shows the contrast for the intensity at 687 nm (red) and 826 nm (pink) integrated in different time-windows with fixed width (250 ps) and variable delay (from 0 ps to 2250 ps) for a channel placed in the left hemisphere. At early time-gates (panels 1 and 2 in Fig. 10) we can observe at both wavelengths a feature, not task related, that disappears when later time-gates are considered. This phenomenon can be attributed to superficial changes in light intensity possibly originated by systemic activities in the scalp or incorrect light coupling between optodes (i.e. stray light). In the late time-gates the modulation in the intensity due to the task is clearly seen instead (with opposite changes for the two wavelengths, as expected).
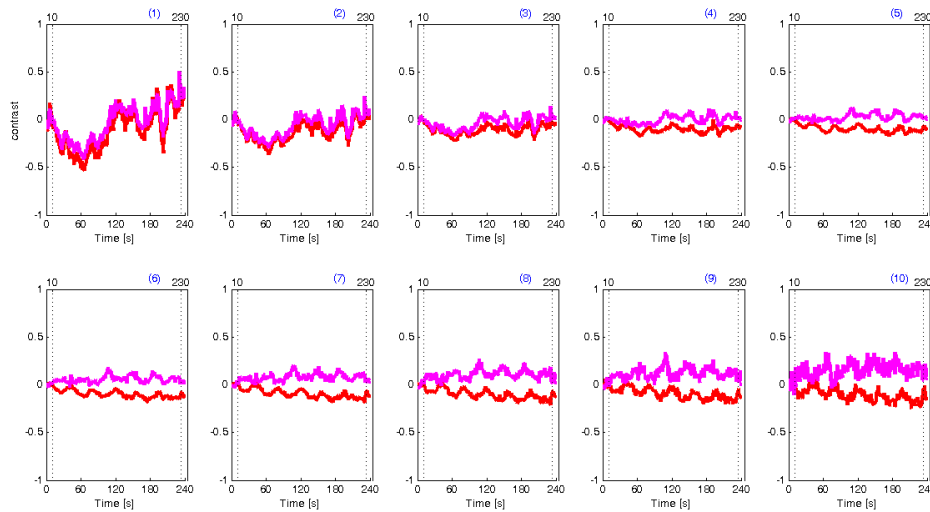

Fig. 10. Contrast for the intensity at 687 nm (red) and 826 nm (pink) integrated in different time-windows with fixed width (250 ps) and variable delay (panel 1 to 10: from 0 ps to 2250 ps) for a channel placed in the left hemisphere.

Figure 11 reports the same data for a channel placed in the right hemisphere. As expected in the late time-gate there is no evidence of the task related modulation being in the ipsilateral hemisphere. Minor changes with slow frequency are observed during the experiment. At 826 nm the contrast is almost the same for all time-gates, suggesting a superficial origin, while at 687 nm the contrast slightly increases at later time-gates, therefore indicating a deeper origin (e.g. cortical hemodynamic changes, not task related).
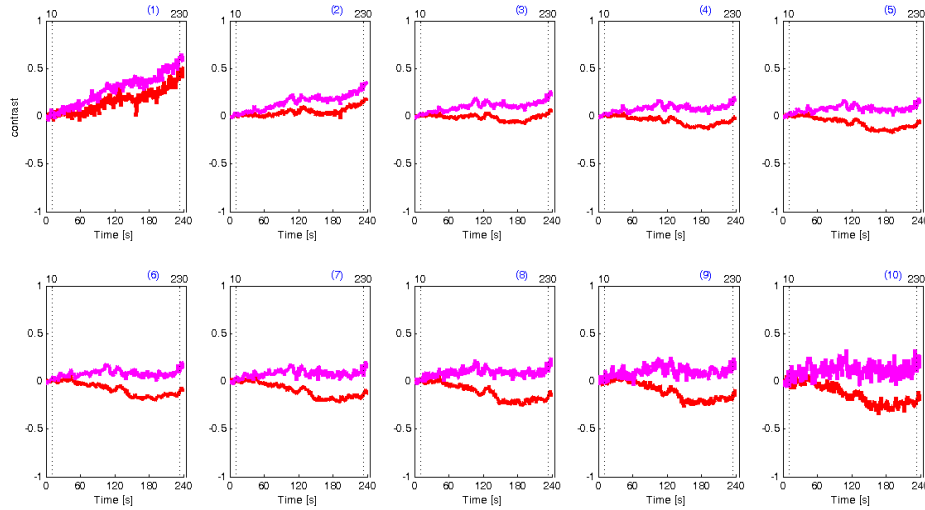
Fig. 11. Contrast for the intensity at 687 nm (red) and 826 nm (pink) integrated in different time-windows with fixed width (250 ps) and variable delay (panel 1 to 10: from 0 ps to 2250 ps) for a channel placed in the right hemisphere.

Figure 12 shows the time course of O$_2$Hb and HHb (obtained by considering only the intensity integrated in late time-gates from 1250 ps to 2000 ps, corresponding to panel from 6 to 9 in Fig. 10) for all the 24 recorded channels. Each channel, i.e. measurement point, is plotted in the position roughly corresponding to the location on the head to create a map for an easier comparison of the changes in the two hemispheres. We can notice an evident cortical activation (increasing in O$_2$Hb, decrease in HHb) and a task related modulation for the contralateral hemisphere (left). In the ipsilateral one (right) we observe less evident changes for the hemoglobins but with strongly reduced task related modulation, as expected during a motor task. We observe that there are slow changes in both O$_2$Hb and HHb during the experiment.
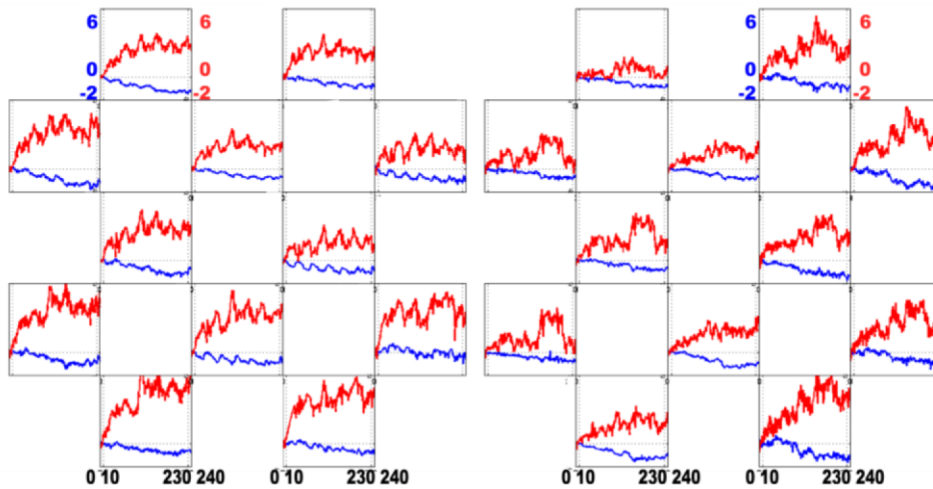

Fig. 12. Time courses (units: μs) of O$_2$Hb (red) and HHb (blue) concentration changes (units: μM) during the experiment for the right and left hemisphere.

To better appreciate the changes during the task, in Fig. 13, we report the maps obtained after folding average of the 6 blocks. For clarity we omit to display the error bars over the repetitions since the dispersion of data is clearly observable in Fig. 12
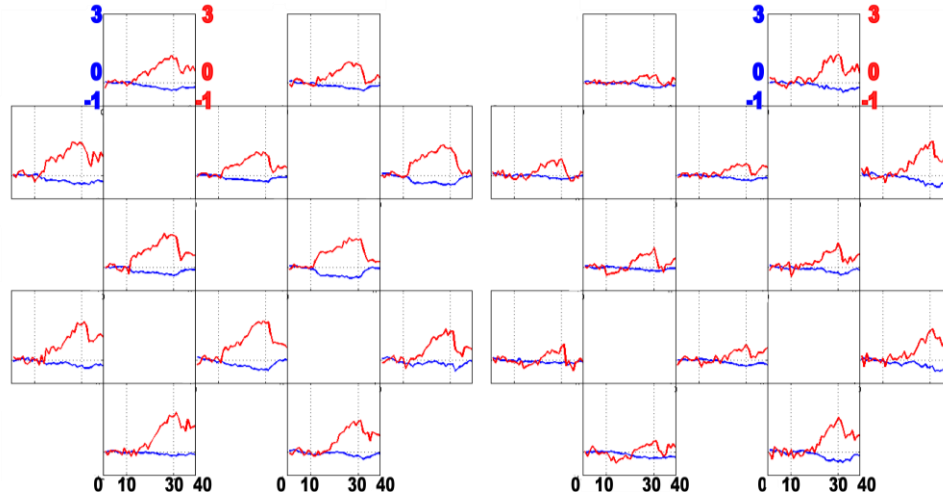
Fig. 13. Time courses (units: µs) of O$_2$Hb (red) and HHb (blue) concentration changes (units: µM) during the experiment (folding average of the 6 blocks) for the right and left hemisphere.

An increase in O$_2$Hb and a corresponding not symmetric decrease in HHb can be noticed in the contralateral (left) hemisphere during the task around C3 point. In the ipsilateral (right) hemisphere there are no task related changes for HHb around C4 point; O$_2$Hb shows minor changes, concentrated mainly in the final part of the task, which however are not statistically correlated with the task, as shown in the next paragraph.

Finally, statistical analysis of the results was performed by means of a general linear model (GLM) approach in the NIRS-SPM software [41, 42]. Figure 14 shows statistical parametric maps (SPM) for O$_2$Hb and HHb concentrations (p<0.001, uncorrected). The regressors and the design matrix were constructed so that the cortical activation was indicated by an increase for O$_2$Hb concentration change and by a corresponding decrease for HHb concentration change. The color-bars represent the significance level of the activation. These maps confirm what we had already found with the visual analysis of the time courses for both the hemispheres. The hemodynamic response is statistically present in the left (contralateral) hemisphere, while the right (ipsilateral) hemisphere does not show statistically significant changes (except for O$_2$Hb, in one channel with a relatively high p-value).
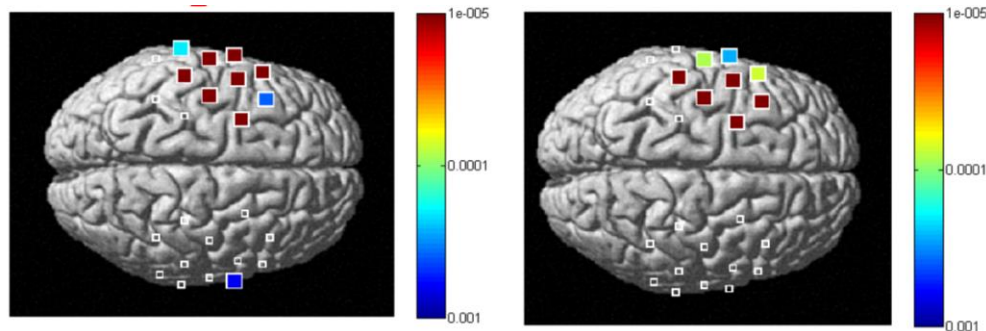

Fig. 14. SPM maps of the cortical activations for O$_2$Hb (left) and HHb (right). p<0.001, uncorrected. The color bars represent the p-value.

5. Conclusions

We have developed and characterized the first TD fNIRS multichannel (16x8) system based on the wavelength space multiplexing approach, which can be used for imaging purpose. This new approach allows to increase the signal-to-noise ratio and reduce the wavelength cross-

talk with respect to the existing instruments based on the wavelength time multiplexing scheme. Moreover, in the acquisition TCSPC chains we have adopted newly developed hybrid photomultipliers with reduced after-pulsing background and we have avoided the use of electronic routers to multiplex the signals from different channels, so as to increase the overall dynamic range. The number of channels available allows the employment of this device both for monitoring muscle or brain oxygenation and functional brain studies in research laboratories. Furthermore, the instrumentation design, based on independent modules dedicated to specific tasks and arranged in a 19" rack case, makes somehow straightforward to obtaining the necessary authorizations for using it also on patients in a clinical environment.

Future work will consist in the introduction of some technical improvements such as the employment of new laser sources with a more stable behavior and a higher power. This will allow, from one side, to reduce the instrument warm-up time and, on the other side, to substitute the fiber bundles adopted for signal collection with single fibers, improving in this way the temporal resolution of the instrument.